# Segment Noncoherent Integration Based Inverse Synthetic Aperture Radar Imaging under Low Signal-to-Noise Ratio

**Jianzhi Lin\*, Yue Zhang, Weixing Li, and Zengping Chen**

**Abstract**—In this paper, a novel scheme for inverse synthetic aperture radar (ISAR) imaging under low signal-to-noise ratio (SNR) condition is proposed. The method is a preprocess of the high-resolution range profiles and relies on the oversampling in the azimuth direction. It divides the entire coherent processing interval into segments according to the down sampling factor. In each segment, original low SNR echoes are noncoherently integrated to obtain a new high SNR echo. With the new high SNR echoes, conventional methods for ISAR imaging can perform much better and obtain a better focused ISAR image. The presented algorithm has the advantage of effectiveness under low SNR condition and computational efficiency. Experimental results based on both the simulated and real radar data of an airplane verify the superiority of the proposed strategy.

## 1. INTRODUCTION

Owing to its ability to provide 2D high-resolution images of moving targets, inverse synthetic aperture radar (ISAR) is widely used in many military and civil fields. However, strong noise has great influence on ISAR imaging by disturbing the range alignment and defocusing the ISAR image. Thus, the study of ISAR imaging techniques under low signal-to-noise ratio (SNR) condition is important.

Translational motion compensation (TMC), the essential procedure for ISAR imaging, generally consists of range alignment and phase adjustment, which compensate range shift and phase error, respectively. Range alignment is a precursor to phase adjustment. Maximum correlation based methods [1, 2] may fail under low SNR condition because of the weakened correlation of the high-resolution range profiles (HRRPs) due to the strong noise. Some robust optimization-based methods [3–5] still have not made a contribution to suppress the noise in the range cell. On the contrary, phase adjustment [6–11] contains the accumulation of the phase of the HRRPs and suppresses the noise in the Doppler cell. Hence, the improvement of range alignment is the bottleneck under low SNR condition. Joint correction methods for simultaneous range alignment and phase adjustment have also been proposed based on a polynomial model of the translational range history, which have the advantage of high SNR gain from 2D coherent integration [11-15]. However, for long coherent processing interval (CPI), the order of the polynomial should be high enough to model the real motion, which causes high computational complexity. A pseudomatched-filter-based (PMF) method [16] is able to suppress the noise in the HRRP envelope, but the correct behavior is dependent on coarse range alignment, which is not realizable under extremely low SNR condition.

Usually, the ISAR system is oversampled in the azimuth direction. For computational efficiency, down sampling is usually adopted by conventional methods. In this article, the redundant echoes are noncoherently integrated to form high SNR echoes. First, the entire CPI is divided into many segments with short CPI. Then in each segment, joint correction is carried out to compensate the translational motion. Since the CPI is short, low order polynomial model is reliable. Consequently, the noncoherent

integration is able to be implemented. Thus, it improves the SNR of the HRRP, and is of computational efficiency and robustness. Finally, conventional techniques are able to reconstruct the ISAR image with the new high SNR echoes. Both simulated and experimental validations are presented to verify the performance of the scheme.

The remainder of the article is organized as follows: the signal model is presented in Section 2; the segment noncoherent integration based ISAR imaging method under low SNR condition is proposed in Section 3; simulated and experimental results are illuminated in Section 4; and conclusions are summarized in Section 5.

## 2. SIGNAL MODEL

Assume that the radar transmits a waveform

$$s_{\mathrm{T}}(\tau, t_m) = p(\tau)\exp(j2\pi f_{\mathrm{c}}t), \tag{1}$$

where $p(\tau)$ is the complex envelope of the transmitted signal, $\tau$ the fast time, $t_m$ the slow time, $t$ the whole time, and $f_c$ the carrier frequency. In addition, $t = \tau + t_m = \tau + mT_r$, $(m = 0, 1, \ldots, M-1)$, where $T_r$ is the pulse repetition interval (PRI) and $MT_r$ is the CPI.

After down-conversion to the baseband and matched-filtering, the target echo can be expressed as

$$S(f, t_m) = |P(f)|^2 \sum_{k=1}^{K} a_k \exp\left[-j2\pi f \frac{2R_k(t_m)}{c}\right]\exp\left[-j2\pi f_{\mathrm{c}}\frac{2R_k(t_m)}{c}\right], \tag{2}$$

where $P(f)$ is the Fourier transform of $p(\tau)$. $K$ is the total number of scatterers. $a_k$ and $R_k(t_m)$ denote the scattering coefficient and distance of the $k$th scatterer corresponding to $t_m$, respectively. $c$ is the wave propagation velocity.

In the ISAR scenario, the target motion can be divided into translation and rotation as follows [14]:

$$R_k(t_m) = R_o(t_m) + x_k\sin\theta(t_m) - y_k\cos\theta(t_m) \approx R_o(t_m) + x_k\omega t_m - y_k, \tag{3}$$

where $R_o(t_m)$ denotes instantaneous distance from radar to the target center, usually representing the translational motion. $(x_k, y_k)$ is the position of the $k$th scatterer with $x_k$ the cross range and $y_k$ the down range. $\theta(t_m)$ is the instantaneous rotation angle. $\omega$ is the effective rotational velocity during the CPI.

By substituting Eq. (3) into Eq. (2), we have

$$\begin{aligned} S(f, t_m) = {} & |P(f)|^2 \exp\left[-j2\pi f \frac{2R_o(t_m)}{c}\right]\exp\left[-j2\pi f_{\mathrm{c}}\frac{2R_o(t_m)}{c}\right] \\ & \cdot \sum_{k=1}^{K} a_k \exp\left(-j2\pi f\frac{2x_k\omega t_m}{c}\right)\exp\left(-j2\pi f_c\frac{2x_k\omega t_m}{c}\right)\exp\left(j2\pi f\frac{2y_k}{c}\right)\exp\left(j2\pi f_c\frac{2y_k}{c}\right) \end{aligned} \tag{4}$$

In Eq. (4), the first exponential term causing misalignment of HRRP in the range-compressed domain needs range alignment. And the second exponential term standing for the phase error from translational motion requires phase adjustment. They are just two typical steps of the TMC. Eq. (4) shows that both the range migration and phase error correspond to the translational motion $R_o(t_m)$, that is why joint correction methods for simultaneous range alignment and phase adjustment can be applied.

In the joint correction methods, the translational motion is modeled as a $Q$-order polynomial:

$$R_o(t_m) = \sum_{q=0}^{Q} \alpha_q t_m^q, \tag{5}$$

where $\alpha_0$ is the initial distance, and $\alpha_1$ physically represents the radial velocity. After the joint correction and neglecting the inessential terms, the motion compensated signal can be obtained as

$$\begin{aligned} S_{\mathrm{MC}}(f, t_m) = {} & |P(f)|^2 \exp\left(-j2\pi f\frac{2\alpha_o}{c}\right)\exp\left(-j2\pi f_{\mathrm{c}}\frac{2\alpha_o}{c}\right) \\ & \cdot \sum_{k=1}^{K} a_k \exp\left(-j2\pi f_c\frac{2x_k\omega t_m}{c}\right)\exp\left(j2\pi f\frac{2y_k}{c}\right). \end{aligned} \tag{6}$$

Finally, the ISAR image formation can be obtained by 2D Fourier transform as

$$
\text{ISAR}\,(\tau, f_D) \triangleq \exp\left(-\mathrm{j}2\pi f_{\mathrm{c}}\frac{2\alpha_o}{c}\right) \sum_{k=1}^{K} a_k psf\left(\tau - \frac{2\alpha_o}{c} + \frac{2y_k}{c}\right)\delta\left(f_D + \frac{2f_c x_k \omega}{c}\right),
\tag{7}
$$

where $psf(\tau)$ is the inverse Fourier transform of $|P(f)|^2$ and $\delta(\cdot)$ the Dirac function. This result clearly shows that the resulting 2D image data are on the time lag-Doppler frequency plane. One dimension is the time lag axis that is proportional to the down range axis, and the other is the Doppler frequency axis that is proportional to the cross range axis. The down range resolution $\rho_r$ and cross range resolution $\rho_a$ are determined by:

$$
\begin{cases} \rho_r = \frac{c}{2B} \\ \rho_a = \frac{\lambda}{2\omega MT_r} \end{cases},
\tag{8}
$$

where $B$ is the bandwidth and $\lambda$ the wavelength. Usually the CPI is chosen to make $\rho_a$ close to $\rho_r$.

## 3. SEGMENT NONCOHERENT INTEGRATION BASED ISAR IMAGING METHOD

Generally the ISAR system is oversampled in the azimuth direction because of slow variation of radar viewing angle and a high PRF. The oversampling factor $o$ can be determined by [1]

$$
o = \frac{cF_r}{2f_c\omega L_x},
\tag{9}
$$

where $F_r$ is the PRF and $L_x$ the azimuth length of the target.

To remove the oversampling to leave minimum useful data, down sampling is usually done to reduce the data rate, which samples at a correspondingly low rate. In order to satisfy the sampling theorem, the down sampling factor $\Delta M$ should be

$$
1 \le \Delta M \le o.
\tag{10}
$$

After the down sampling, the new oversampling factor $\tilde{o}$ will be

$$
\tilde{o} = \frac{o}{\Delta M} = \frac{cF_r/\Delta M}{2f_c\omega L_x}.
\tag{11}
$$

For the quality of the resultant image, the down sampling factor $\Delta M$ should be selected such that the new oversampling factor $\tilde{o}$ is equivalent to its empirical values 2–5.

The down sampling can be regarded as dividing the entire CPI into segments by the factor $\Delta M$ and selecting only one echo from each segment. In our proposed method, noncoherent integration is carried out in each segment instead.

Assume that the entire CPI $MT_r$ is divided into $L$ segments by the factor $\Delta M$. Therefore, the CPI in each segment is $\Delta MT_r$, which means that the criteria for selecting the length of the noncoherent pulse train is the same with that for selecting the down sampling factor. According to Eq. (4), the signal in the $l$th segment can be written as

$$
S\,(f, t_{lm}) = |P\,(f)|^2 \exp\left[-\mathrm{j}2\pi f\frac{2R_o\,(t_{lm})}{c}\right]\exp\left[-\mathrm{j}2\pi f_{\mathrm{c}}\frac{2R_o\,(t_{lm})}{c}\right]
$$

$$
\cdot \sum_{k=1}^{K} a_k \exp\left(-\mathrm{j}2\pi f\frac{2x_k\omega t_{lm}}{c}\right)\exp\left(-\mathrm{j}2\pi f_c\frac{2x_k\omega t_{lm}}{c}\right)\exp\left(\mathrm{j}2\pi f\frac{2y_k}{c}\right)\exp\left(\mathrm{j}2\pi f_c\frac{2y_k}{c}\right)
\tag{12}
$$

where $t_{lm} = l\Delta MT_r, l\Delta MT_r + T_r, l\Delta MT_r + 2T_r, \ldots, l\Delta MT_r + (\Delta M - 1)T_r$, and $l = 0, 1, \ldots, L - 1$.

For such short CPI, the translational motion can be modeled as a low order polynomial. Therefore the TMC can be efficiently achieved by joint correction. Consequently, according to Eq. (6) the compensated signal is expressed as

$$
S_{\mathrm{MC}}\,(f, t_{lm}) = |P\,(f)|^2 \exp\left(-\mathrm{j}2\pi f\frac{2\alpha_{l0}}{c}\right)\exp\left(-\mathrm{j}2\pi f_c\frac{2\alpha_{l0}}{c}\right)
$$

$$
\cdot \sum_{k=1}^{K} a_k \exp\left(-\mathrm{j}2\pi f_c\frac{2x_k\omega t_{lm}}{c}\right)\exp\left(\mathrm{j}2\pi f\frac{2y_k}{c}\right),
\tag{13}
$$

where $\alpha_{l0}$ is the initial distance for the $l$th segment, such that $\alpha_{l0} = R_o(l\Delta M T_r)$.

After the range compression by inverse Fourier transform with respect to $f$, and considering the inevitable noise, the HRRP of the $l$th segment can be represented as

$$s_{\mathrm{MC}}(\tau, t_l, t_{\Delta m}) = \exp\left[-\mathrm{j}2\pi f_{\mathrm{c}}\frac{2R_o(t_l)}{c}\right]\sum_{k=1}^{K} a_k psf\left[\tau - \frac{2R_o(t_l)}{c} + \frac{2y_k}{c}\right]\exp\left(-\mathrm{j}2\pi f_{\mathrm{c}}\frac{2x_k\omega t_l}{c}\right)$$
$$\cdot \exp\left(-\mathrm{j}2\pi f_{\mathrm{c}}\frac{2x_k\omega t_{\Delta m}}{c}\right) + w_1(\tau, t_l, t_{\Delta m}), \tag{14}$$

where $t_l = l\Delta M T_r$ and $t_{\Delta m} = \Delta m T_r$, $(\Delta m = 0, 1, \ldots, \Delta M - 1)$. $w_1$ is the zero-mean complex noise.

Hence, noncoherent integration can be obtained by magnitude accumulation as follows:

$$|s_{\mathrm{NCI}}(\tau, t_l)| = \sum_{\Delta m=0}^{\Delta M-1} |s_{\mathrm{MC}}(\tau, t_l, t_{\Delta m})| = \eta\sum_{k=1}^{K} a_k psf\left[\tau - \frac{2R_o(t_l)}{c} + \frac{2y_k}{c}\right] + w_2(\tau, t_l), \tag{15}$$

where $\eta$ indicates the improvement in the SNR, and $w_2$ is the zero-mean complex noise. As for the noncoherent integration, Eq. (15) improves the SNR by about $(\Delta M)^{0.7}$ when $\Delta M$ is small, or $0.5(\sqrt{\Delta M})$ when $\Delta M$ is large.

Note that the noncoherent integration result in Eq. (15) is only useful for the envelope of the new HRRP. The phase of some HRRP in the segment before noncoherent integration, e.g., the first one, should be multiplied by the envelope to rebuild the complex HRRP as follows:

$$s_{\mathrm{NCI}}(\tau, t_l) = |s_{\mathrm{NCI}}(\tau, t_l)| \cdot \exp\{\mathrm{j}\cdot angle[s_{\mathrm{MC}}(\tau, t_l, t_{\Delta m})|_{\Delta m=0}]\}$$
$$= \eta\exp\left[-\mathrm{j}2\pi f_{\mathrm{c}}\frac{2R_o(t_l)}{c}\right]\sum_{k=1}^{K} a_k psf\left[\tau - \frac{2R_o(t_l)}{c} + \frac{2y_k}{c}\right]\exp\left(-\mathrm{j}2\pi f_{\mathrm{c}}\frac{2x_k\omega t_l}{c}\right) + w_3(\tau, t_l), \tag{16}$$

where $w_3$ is the zero-mean complex noise. Eq. (16) seems like the signal after down sampling by the factor $\Delta M$, but the SNR is improved now. From Eq. (16), we can see that $L$ segments form $L$ new high SNR echoes and $R_o(t_l)$ causes the range migration and phase error. Since the SNR is high now, TMC can be achieved by conventional methods. After the TMC, the signal can be written as

$$s_{\mathrm{NCI\_MC}}(\tau, t_l) = \eta\exp\left(-\mathrm{j}2\pi f_{\mathrm{c}}\frac{2\alpha_o}{c}\right)\sum_{k=1}^{K} a_k psf\left(\tau - \frac{2\alpha_o}{c} + \frac{2y_k}{c}\right)\exp\left(-\mathrm{j}2\pi f_{\mathrm{c}}\frac{2x_k\omega t_l}{c}\right) + w_4(\tau, t_l), \tag{17}$$

where $w_4$ is the zero-mean complex noise.

Finally, the ISAR image can be reconstructed by Fourier transform with respect to $t_l$ as

$$ISAR(\tau, f_D) \triangleq \eta\exp\left(-\mathrm{j}2\pi f_{\mathrm{c}}\frac{2\alpha_o}{c}\right)\sum_{k=1}^{K} a_k psf\left(\tau - \frac{2\alpha_o}{c} + \frac{2y_k}{c}\right)\delta\left(f_D + \frac{2f_{\mathrm{c}}x_k\omega}{c}\right) + w_5(\tau, f_D), \tag{18}$$

where $w_5$ is the zero-mean complex noise.

Equation (18) is identical to Eq. (7) except for a constant factor, which has no relevance since normalization is carried out in practice.

For clarity, we present a flowchart of the presented method in Fig. 1.

From the flowchart we can make an easy analysis on the complexity between the proposed method and entire CPI-based method. If the entire CPI-based method adopts joint correction for the TMC and the translational motion is modeled as a $Q$-order polynomial, its complexity would be $(2\alpha_{\max}/\Delta\alpha)^{(Q-1)}$ times more than that of the proposed method ($[-\alpha_{\max}, \alpha_{\max}]$ is the exhaustive search range and $\Delta\alpha$ is the search step for the rough estimation of the polynomial parameters). If the entire CPI-based method adopts conventional methods for the TMC, its complexity would be $2\alpha_{\max}/\Delta\alpha$ times less than that of the proposed method. However, it might fail to reconstruct the ISAR image under low SNR condition. Hence, the proposed method has the advantage of effectiveness under extremely low SNR condition and computational efficiency.
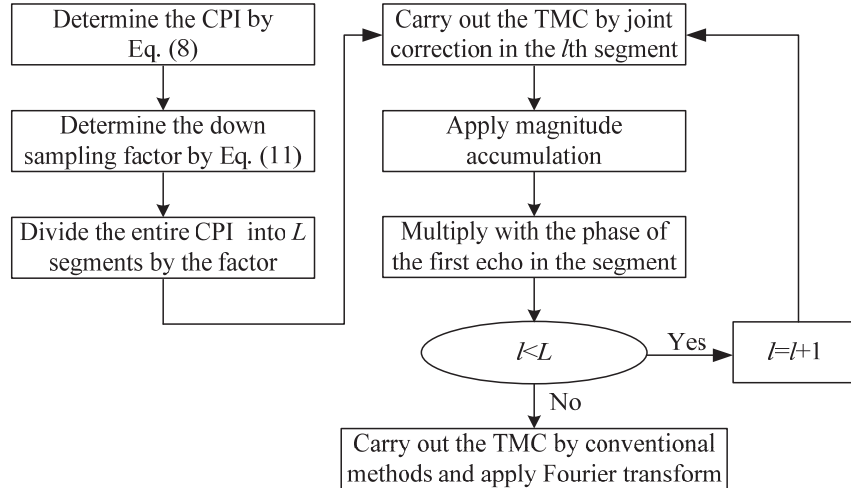
```
┌─────────────────────┐        ┌─────────────────────────┐
│  Determine the CPI  │        │ Carry out the TMC by    │◄──────┐
│  by Eq. (8)         │   ┌───►│ joint correction in the │       │
└─────────┬───────────┘   │    │ lth segment             │       │
          │               │    └───────────┬─────────────┘       │
          ▼               │                ▼                     │
┌─────────────────────┐   │    ┌─────────────────────────┐       │
│  Determine the down │   │    │  Apply magnitude        │       │
│ sampling factor by  │   │    │  accumulation           │       │
│ Eq. (11)            │   │    └───────────┬─────────────┘       │
└─────────┬───────────┘   │                ▼                     │
          │               │    ┌─────────────────────────┐       │
          ▼               │    │ Multiply with the phase │       │
┌─────────────────────┐   │    │ of the first echo in    │       │
│ Divide the entire   │   │    │ the segment             │       │
│ CPI into L segments │───┘    └───────────┬─────────────┘       │
│ by the factor       │                    ▼                     │
└─────────────────────┘              ╱──────────╲    Yes    ┌─────────┐
                                    │    l<L     │──────────►│ l=l+1   │
                                     ╲──────────╱           └─────────┘
                                          │ No
                                          ▼
                              ┌─────────────────────────────┐
                              │ Carry out the TMC by         │
                              │ conventional methods and     │
                              │ apply Fourier transform      │
                              └─────────────────────────────┘
```

**Figure 1.** Flowchart of the presented method.

## 4. EXPERIMENTAL VERIFICATION AND ANALYSIS

In this section, simulated data of a facet model of an airplane as well as real radar measurement data of an aircraft are used to evaluate the performance of the proposed algorithm.

In the simulation, physical optics facet model is used to calculate radar backscattering from the simulated target. Since the resolution comes to a few decimeters and the target motion is in fact complex, 4-order polynomial motion is considered to be existed in real conditions for long CPI and is consequently added into the backscattering data. The simulation parameters including the radar characteristics and the target motion quantities are shown in Table 1.

**Table 1.** Simulation parameters.

| | |
|---|---|
| Carrier frequency | $10\,\mathrm{GHz}$ |
| Bandwidth | $1\,\mathrm{GHz}$ |
| Pulse repetition frequency | $500\,\mathrm{Hz}$ |
| Range cell numbers | 512 |
| $\alpha_0$ | $50\,\mathrm{km}$ |
| $\alpha_1$ | $50\,\mathrm{m/s}$ |
| $\alpha_2$ | $5\,\mathrm{m/s^2}$ |
| $\alpha_3$ | $0.05\,\mathrm{m/s^3}$ |
| $\alpha_4$ | $0.0005\,\mathrm{m/s^4}$ |
| Rotation velocity | $0.35\,\mathrm{deg/s}$ |
| azimuth length | $18\,\mathrm{m}$ |

According to the parameters and Eq. (8), the radar system provides a range resolution of $0.15\,\mathrm{m}$. In order to achieve an equivalent cross range resolution, the CPI should be about $16.37\,\mathrm{s}$ according to Eq. (8), which means that about 8192 echoes are needed. Then according to Eq. (9), the oversampling factor is as high as 68. Hence, the down sampling factor can be chosen as 32 according to Eq. (11). Therefore after the segment noncoherent integration the SNR will be improved by about 3, i.e., $5\,\mathrm{dB}$.

Figure 2(a) plots the entire HRRP time history. It can be easily noted that the stripes are largely crooked, which indicates a high order translation motion. Figure 2(b) shows the SNR of the HRRP, from which we can see that the SNR is about $16\,\mathrm{dB}$.
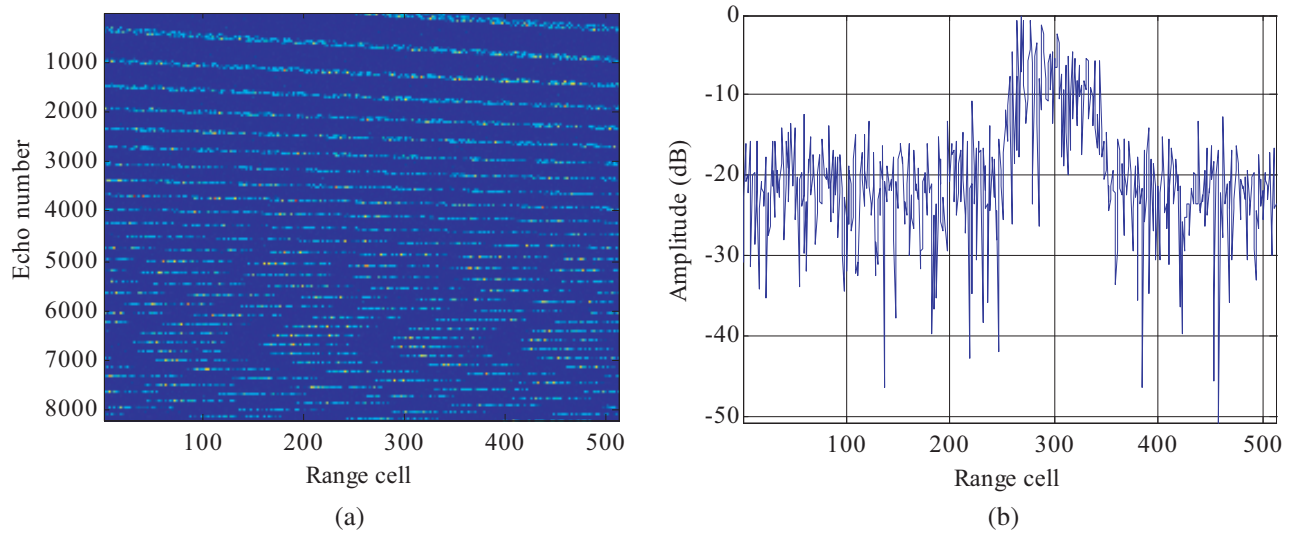
**Figure 2.** HRRP: (a) Entire HRRP time history and (b) SNR of the HRRP.

According to the CPI and down sampling factor, 256 segments are achieved. Figure 3(a) plots the HRRP time history of the first segment. It can be easily noted that the stripes are almost linear, which means that a low order polynomial model is enough to characterize the translation motion. After the joint correction and noncoherent integration, the result is shown in Figure 3(b), from which we can see that the SNR is about 21 dB. Hence, an improvement of about 5 dB is achieved.
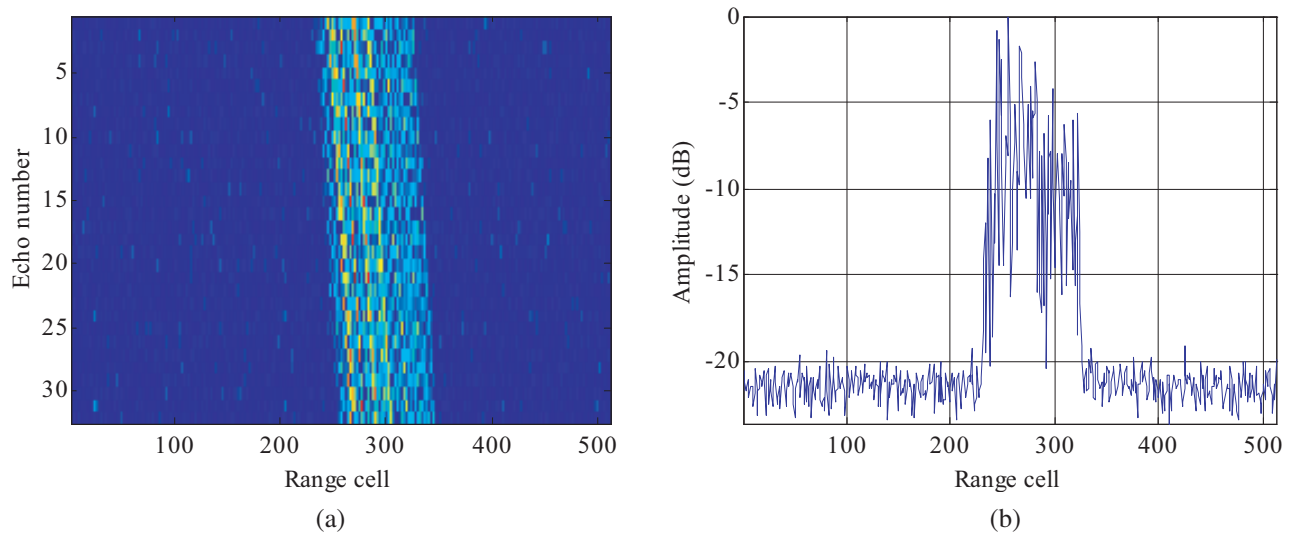


**Figure 3.** HRRP: (a) HRRP time history of the first segment and (b) SNR of the HRRP after noncoherent integration.

All the HRRPs after segment noncoherent integration form the new HRRP time history as shown in Figure 4(a). In Figure 4(b), the HRRP time history after down sampling is plotted. Figure 4(a) and Figure 4(b) are almost the same except the SNR. We can note that the noise is suppressed, which confirms the denoising ability of the proposed method.

The range alignments achieved by the proposal and global method [4] are shown in Figure 5(a) and Figure 5(b), respectively. And the corresponding ISAR images are presented in Figure 6(a) and Figure 6(b), respectively. Since the SNR is high, both methods obtain perfectly range alignment and
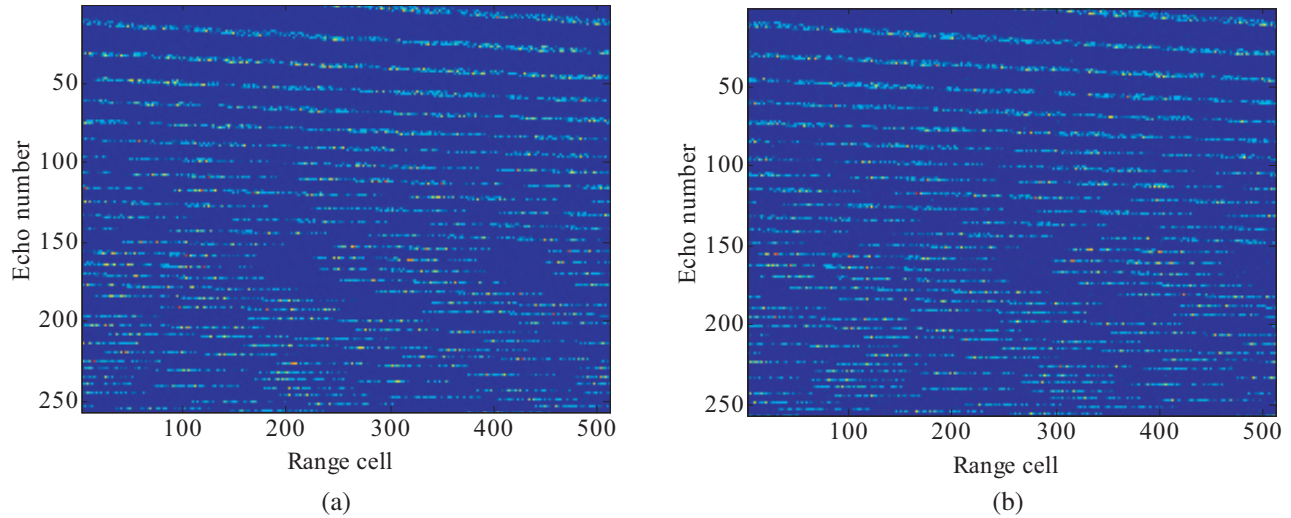
**Figure 4.** HRRP time history: (a) After segment noncoherent integration and (b) after down sampling.
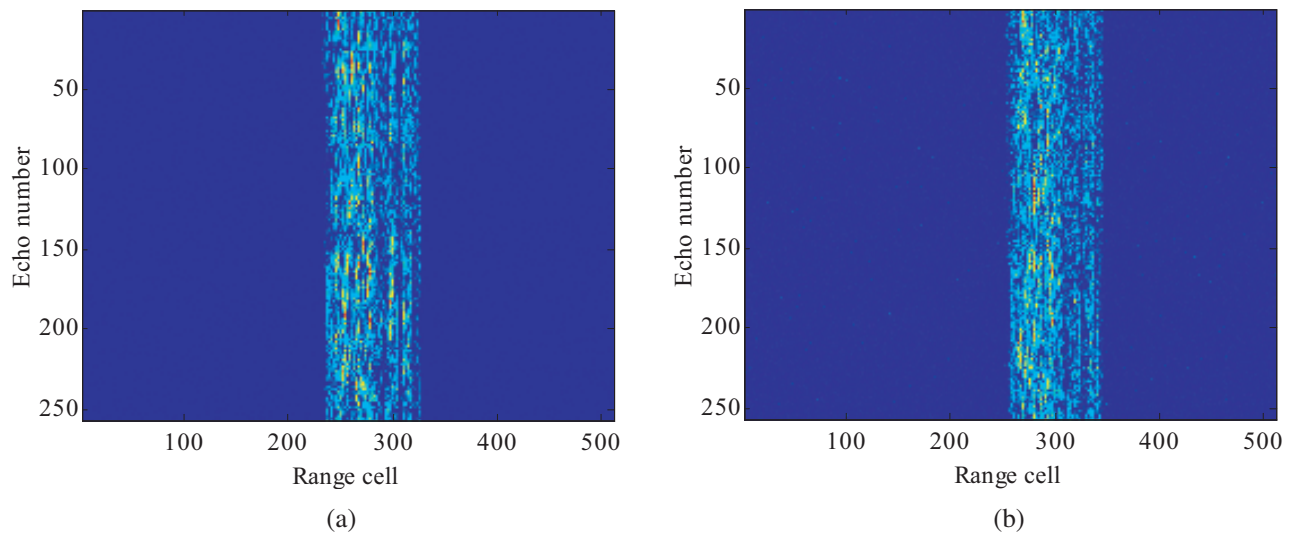


**Figure 5.** Range alignment obtained by: (a) The proposal and (b) global method.

focused ISAR images. Thus, the correctness of the proposed method is validated.

Further, we consider the performance of the proposed algorithm under low SNR condition. We add additive Gaussian white noise with a mean of zero into the signal to make the SNR as low as 5 dB. Here the SNR corresponds to HRRP after pulse compression. For the case of global method, the presence of strong noise disturbs the range alignment as shown in Figure 7(b), leading to blurring and smearing in the ISAR image as shown in Figure 8(b). The proposed method can improve the SNR and therefore the range alignment is more robust as shown in Figure 7(a). Consequently, the ISAR image shown in Figure 8(a) is still clear. Thus, the superiority of the proposed method under low SNR condition is validated.

In addition, the proposed method also outperforms the PMF method in extremely low SNR condition. Figure 9 shows the ISAR images obtained by the PMF method under different SNR conditions. It is obvious that the PMF method fails to reconstruct the ISAR image when the SNR is as low as 5 dB.

Real radar data of an aircraft are utilized to further validate the performance of the proposed algorithm. The aircraft is Boeing 737, which has the length/width/height of 33.6 m/34.3 m/12.5 m,
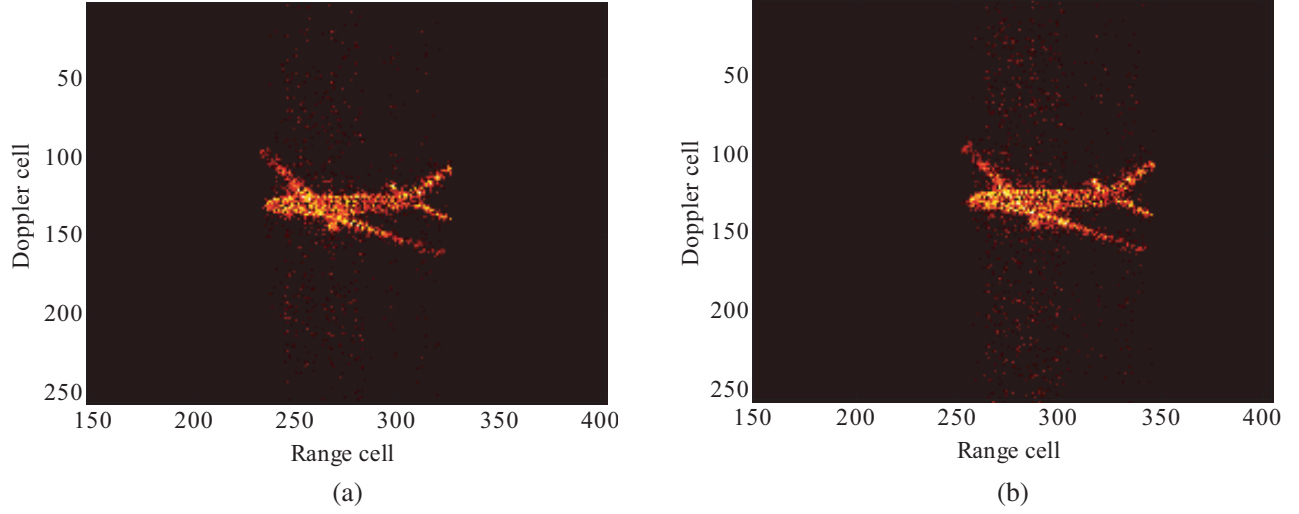
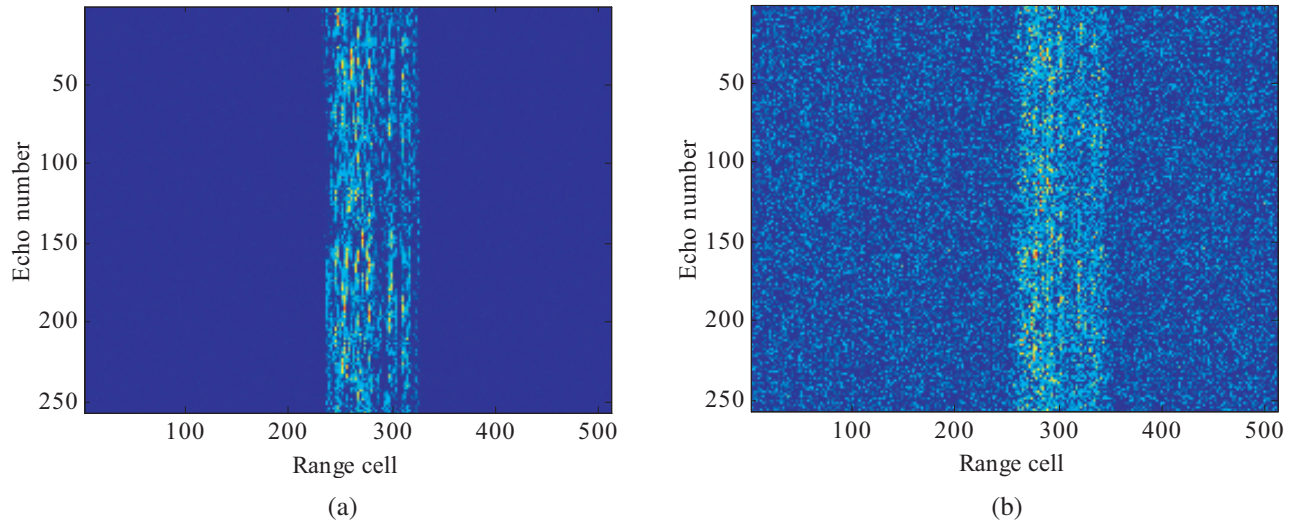**Figure 6.** ISAR images obtained by: (a) The proposal and (b) global method.



**Figure 7.** Range alignment obtained in low SNR by: (a) The proposal and (b) global method.

respectively. The distance between the aircraft and the radar is about 38 km. The aircraft is measured by the X-band radar under field conditions. The parameters of the radar are as follows: the center frequency is 9.5 GHz; the bandwidth is 1 GHz; and the PRI is 3 ms. 512 echoes are used in this experiment. The down sampling factor is determined to be 2, which indicates a 2 dB improvement in the SNR.

The ISAR images are shown in Figure 10 for high SNR case and Figure 11 for low SNR case. They are all plotted in logarithmic scale with the dynamic range of 35 dB. In the first case, both methods can obtain clear ISAR images as shown in Figure 10, which validates the correctness of the proposed algorithm. In the other case, as shown in Figure 11, the global method fails to reconstruct the ISAR image, while the proposed method can still achieve an image with some tolerable noise. This comparison verifies the effectiveness of the presented strategy. Of course, as the down sampling factor is as small as 2, only 2 dB improvement can be obtained. Thus, the results are not very visible. However, we can presume that in the case of large down sampling factor, obvious effectiveness will show up.

For the quantitative analysis of the performance of the methods, we utilize the image entropy and contrast to evaluate the images in Figures 6, 8, 10 and 11, which are presented in Tables 2 and 3,
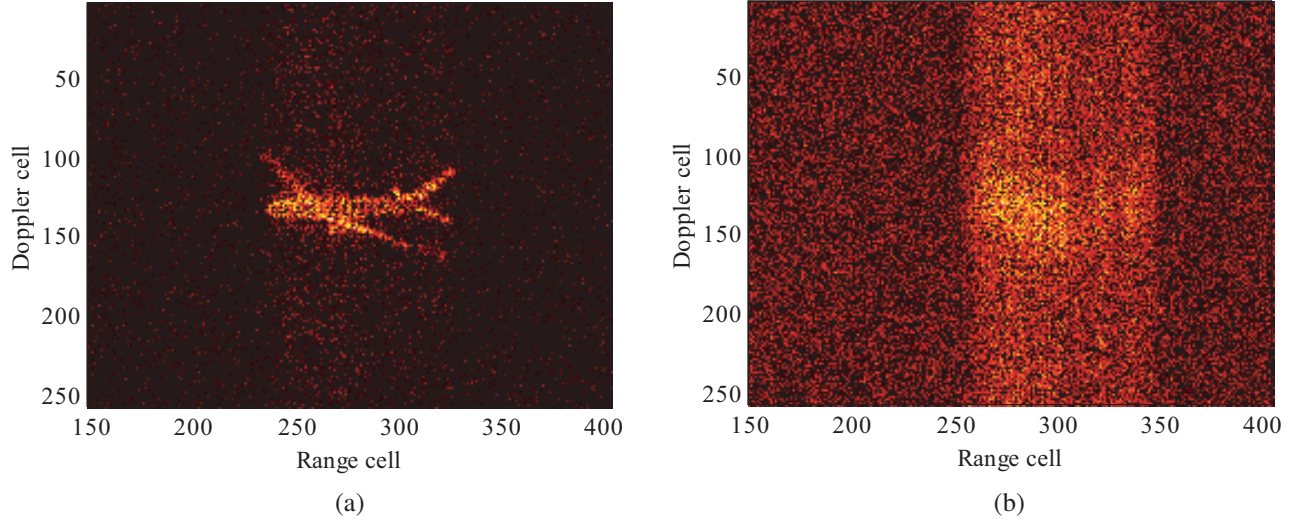
**Figure 8.** ISAR images obtained in low SNR by: (a) The proposal and (b) global method.
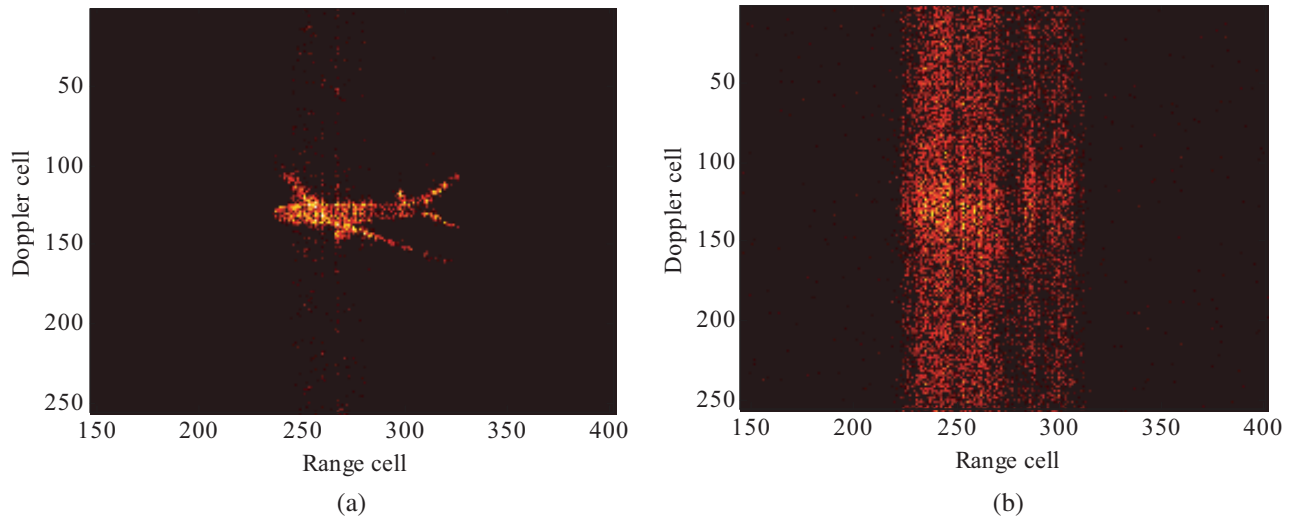


**Figure 9.** ISAR images obtained by PMF under different SNR: (a) 16 dB and (b) 5 dB.

respectively. Here the entropy and contrast are defined as follows [15]:

$$
\begin{cases}
Entropy \triangleq -\sum_{m=0}^{M-1}\sum_{n=0}^{N-1} \dfrac{|I(m,n)|^2}{\displaystyle\sum_{m=0}^{M-1}\sum_{n=0}^{N-1}|I(m,n)|^2} \ln \dfrac{|I(m,n)|^2}{\displaystyle\sum_{m=0}^{M-1}\sum_{n=0}^{N-1}|I(m,n)|^2} \\[2em]
Contrast \triangleq \dfrac{\sqrt{Aver\left\{[|I(m,n)|-Aver\{|I(m,n)|\}]^2\right\}}}{Aver\{|I(m,n)|\}}
\end{cases}, \tag{19}
$$

where $I(m,n)$ is the complex image. $m$ and $n$ are the sequence numbers in azimuth and range, respectively. $Aver\{\cdot\}$ represents the spatial mean over the coordinates $(m,n)$.

It is well known that lower entropy and higher contrast indicate better focused image, and vice versa. As seen from the tables, the proposed method has lower entropy and higher contrast, which indicates better performance of the proposed method.

**Table 2.** Entropy evaluation.

|            | (a) the proposal | (b) global method |
|------------|------------------|-------------------|
| Figure 6   | 8.9016           | 9.0710            |
| Figure 8   | 10.6881          | 11.1408           |
| Figure 10  | 7.8338           | 7.8879            |
| Figure 11  | 10.6166          | 10.7529           |

**Table 3.** Contrast evaluation.

|            | (a) the proposal | (b) global method |
|------------|------------------|-------------------|
| Figure 6   | 1.4569           | 1.3612            |
| Figure 8   | 0.7448           | 0.6275            |
| Figure 10  | 3.0720           | 2.9767            |
| Figure 11  | 0.7468           | 0.7240            |
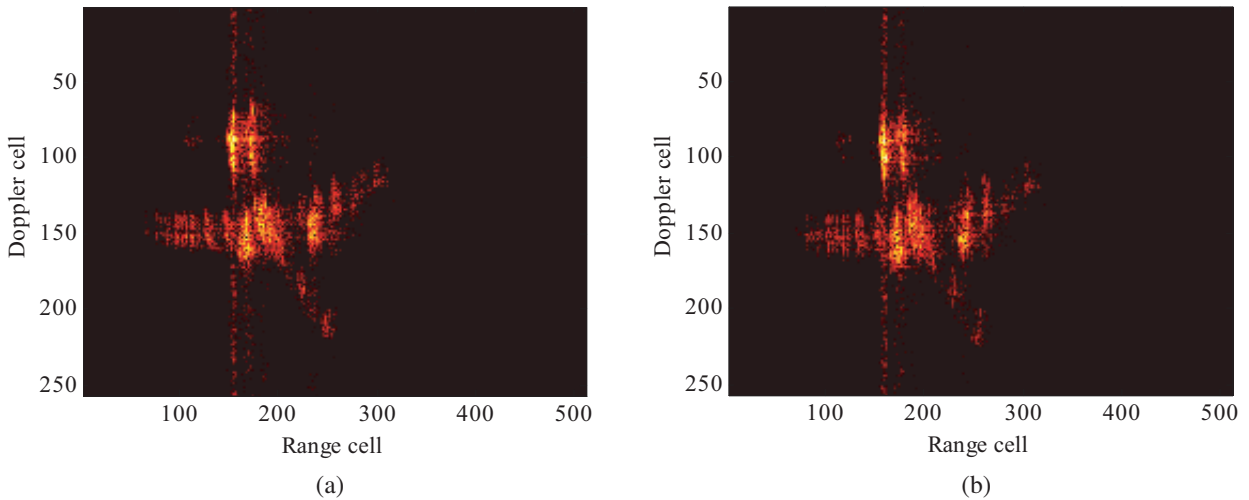


**Figure 10.** ISAR images of a real aircraft obtained by: (a) The proposal and (b) global method.
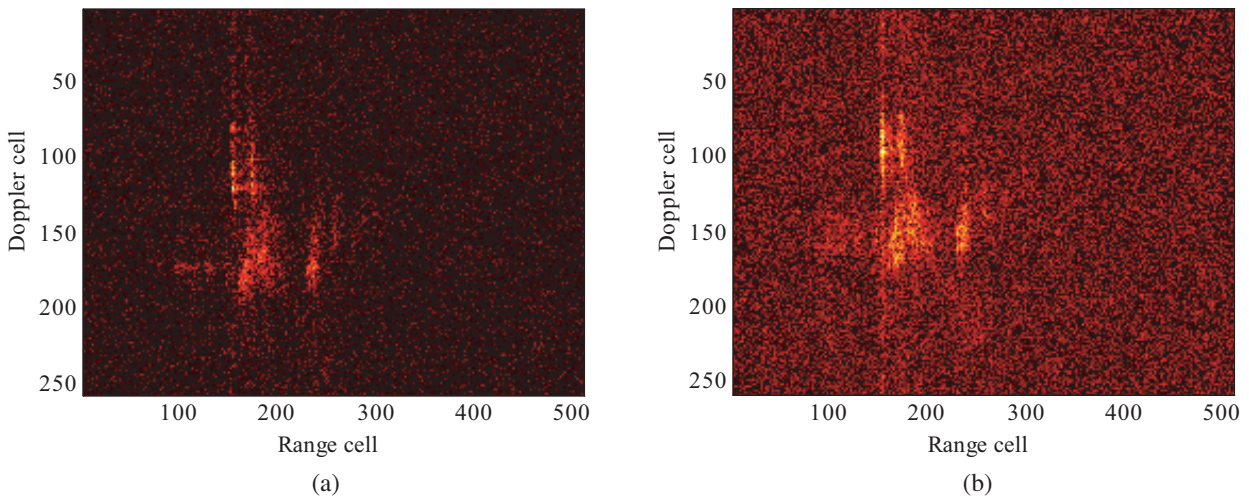


**Figure 11.** ISAR images of a real aircraft obtained in low SNR by: (a) The proposal and (b) global method.

## 5. CONCLUSION

This paper describes a novel ISAR imaging technique under low SNR condition. The scheme is established by segment noncoherent integration to improve the SNR of the HRRP. Therefore, the TMC performs well, and the ISAR image is clear. Results based on simulated and real radar data of an aircraft validate the performance of the proposed algorithm. However, in the case of low PRF, down sampling is inapplicable, and the segment noncoherent integration might fail. Thus, ISAR imaging under low PRF and low SNR condition needs to be further studied.

## REFERENCES

1. Chen, C. C. and H. C. Andrews, "Target-motion-induced radar imaging," *IEEE Transactions on Aerospace and Electronic Systems*, Vol. 16, No. 1, 2–14, 1980.
2. Delise, G. Y. and H. Wu, "Moving target imaging and trajectory computation using ISAR," *IEEE Transactions on Aerospace and Electronic Systems*, Vol. 30, No. 3, 887–889, 1994.
3. Wang, J. and D. Kasilingam, "Global range alignment for ISAR," *IEEE Transactions on Aerospace and Electronic Systems*, Vol. 39, No. 1, 351–357, 2003.
4. Wang, J. and X. Liu, "Improved global range alignment for ISAR," *IEEE Transactions on Aerospace and Electronic Systems*, Vol. 43, No. 3, 1070–1075, 2007.
5. Zhu, D., L. Wang, Y. Yu, Q. Tao, and Z. Zhu, "Robust ISAR range alignment via minimizing the entropy of the average range profile," *IEEE Geoscience and Remote Sensing Letters*, Vol. 6, No. 2, 204–208, 2009.
6. Itoh, T. M. and G. W. Donohoe, "Motion compensation for ISAR via centroid tracking," *IEEE Transactions on Aerospace and Electronic Systems*, Vol. 32, No. 7, 1191–1197, 1996.
7. Ye, W., T. S. Yeo, and Z. Bao, "Weighted least-squares estimation of phase errors for SAR/ISAR autofocus," *IEEE Transactions on Geoscience and Remote Sensing*, Vol. 37, No. 9, 2487–2494, 1999.
8. Eichel, P. H. and C. V. Jakowatz, "Phase-gradient algorithm as an optimal estimator of the phase derivative," *Optics Letters*, Vol. 14, No. 20, 1101–1103, 1989.
9. Huang, D. R., L. Zhang, M. D. Xing, and Z. Bao, "ISAR autofocus method for maneuvering targets," *Journal of Xidian University*, Vol. 41, No. 3, 71–78, 2014.
10. Li, X., G. Liu, and J. Ni, "Autofocusing of ISAR imaging based on entropy minimization," *IEEE Transactions on Aerospace and Electronic Systems*, Vol. 35, No. 4, 1240–1251, 1999.
11. Martorella, M., F. Berizzi, and B. Haywood, "Contrast maximization based technique for 2-D ISAR autofocusing," *IEE Proceedings on Radar, Sonar and Navigation*, Vol. 52, No. 4, 253–262, 2005.
12. Martorella, M., F. Berizzi, and S. Bruscoli, "Use of genetic algorithms for contrast and entropy optimization in ISAR autofocusing," *EURASIP Journal on Applied Signal Processing*, Vol. 2006, No. 87298, 1–11, 2006.
13. Yang, L., T. Xiong, L. Zhang, and M. D. Xing, "Translational motion compensation for ISAR imaging based on joint autofocusing under the low SNR," *Journal of Xidian University*, Vol. 39, No. 3, 63–71, 2012.
14. Zhang, L., J. L. Sheng, J. Duan, M. D. Xing, Z. J. Qiao, and Z. Bao, "Translational motion compensation for ISAR imaging under low SNR by minimum entropy," *EURASIP Journal on Advances in Signal Processing*, Vol. 2013, No. 33, 1–19, 2013.
15. Liu, L., F. Zhou, M. L. Tao, P. G. Sun, and Z. J. Zhang, "Adaptive translational motion compensation method for ISAR imaging under low SNR based on particle swarm optimization," *IEEE Journal of Selected Topics in Applied Earth Observations and Remote Sensing*, Vol. 8, No. 11, 5146–5157, 2015.
16. Zhang, S. H., Y. X. Liu, and X. Li, "Pseudomatched-filter-based ISAR imaging under low SNR condition," *IEEE Geoscience and Remote Sensing Letters*, Vol. 11, No. 7, 1240–1244, 2014.